

# Midinfrared multispectral tissue imaging using a chalcogenide fiber supercontinuum source

**Petersen, Christian Rosenberg; Prtljaga, Nikola ; Farries, Mark; Ward, Jon; Napier, Bruce; Rhys Lloyd, Gavin; Nallala, Jayakrupakar; Stone, Nick; Bang, Ole**

*Published in:*
Optics Letters

*Link to article, DOI:*
10.1364/OL.43.000999

*Publication date:*
2018

*Document Version*
Peer reviewed version

# Mid-infrared multispectral tissue imaging using a chalcogenide fiber supercontinuum source

**Christian Rosenberg Petersen,[1,*] Nikola Prtljaga,[2] Mark Farries,[2] Jon Ward,[2] Bruce Napier,[3] Gavin Rhys Lloyd,[4] Jayakrupakar Nallala,[5] Nick Stone[5], Ole Bang,[1,6]**

[1] *DTU Fotonik, Technical University of Denmark, Ørsteds Plads bldg. 343, DK-2800 Kgs. Lyngby, Denmark.*
[2] *Gooch & Housego, Broomhill Way, Torquay TQ2 2QL, UK.*
[3] *Vivid Components, Dr.-Rörig-Damm 22, 33102 Paderborn, Germany.*
[4] *Biophotonics Research Unit, Gloucestershire Hospitals NHS Foundation Trust, Gloucester, GL1 3NN, UK.*
[5] *Biomedical Physics, School of Physics and Astronomy, University of Exeter, Stocker Road, Exeter, EX4 4QL UK.*
[6] *NKT Photonics A/S, Blokken 84, DK-3460 Birkerød, Denmark.*
**Corresponding author: chru@fotonik.dtu.dk*

**We present the first demonstration of mid-infrared supercontinuum tissue imaging at wavelengths beyond 5 µm using a fiber-coupled supercontinuum source spanning 2-7.5 µm. The supercontinuum was generated in a tapered large mode area chalcogenide photonic crystal fiber in order to obtain broad bandwidth, high average power, and single-mode output for diffraction-limited imaging performance. Tissue imaging was demonstrated in transmission at selected wavelengths between 5.7 µm (1754 $cm^{-1}$) and 7.3 µm (1370 $cm^{-1}$) by point scanning over a sub-mm region of colon tissue, and the results were compared to images obtained from a commercial instrument.**

Mid-infrared (mid-IR) spectral imaging is a promising label-free diagnostic tool that could complement the current method of cancer diagnosis rendered by conventional histopathology. Its capabilities in combination with data mining algorithms have been demonstrated on various types of cancer [1–4], which makes it interesting and relevant for clinical applications. However, conventional mid-IR spectral imaging is based on thermal light sources in combination with Fourier transform infrared (FTIR) spectroscopy, which limits the acquisition speed and penetration depth due to low source brightness and precludes the use of optical fibers for flexible delivery and detection of light. Clinical applications of spectral pathology rely on its ability to compete with current practice and to fit into existing timescales for sample analysis. In this regard, considerable attention has been directed towards utilizing intense laser sources to provide sufficient signal-to-noise ratio (SNR) for rapid acquisition across the mid-IR. Such sources could also have potential for non-destructive reflectance imaging of tissue in vivo [5]. In recent years, several demonstrations of mid-IR imaging using quantum cascade lasers (QCL) has emerged, resulting in a drastic reduction in acquisition time from hours to minutes, and even just a few seconds when operated in a discrete frequency imaging mode [6–9]. However, several QCLs are needed to cover the frequencies that are of diagnostic importance to pathologists, which adds significantly to the cost and complexity of the system.

Another type of laser source that could be useful for mid-IR broadband spectral imaging is the supercontinuum (SC) source [10]. Unlike QCLs, mid-IR SC sources have the potential for providing scan-less access to both the functional group region (~2-6 µm) and part of the fingerprint region (~6-12 µm) from a single monolithic fiber-based source [11,12]. Having access to both the fundamental and overtone vibrational resonances of various molecules allows for more advanced chemometric analytical techniques, such as multitone correlation spectroscopy, which has found application in e.g. food quality control [13]. Previous work on mid-IR SC imaging has been based on $ZrF_4$-$BaF_2$-$LaF_3$-$AlF_3$-NaF (ZBLAN) fiber-based sources, benefitting from the availability of components and maturity of mid-IR technology in the 2-5 µm range [14–16]. In a recent demonstration, such a SC source was used in combination with an acousto-optic tunable filter (AOTF), a Cassegrain transmission microscope, and a 640 x 480 pixel infrared camera to perform hyperspectral imaging of colon tissue from 2.8-3.7 µm [14]. The combination of fast wavelength selection and high signal power enabled capturing of a 100 x 640 x 480 hyperspectral cube in just 2 seconds, which is fast enough to perform real-time measurements for clinical applications.

In this letter we present the first proof-of-principle demonstration of mid-IR supercontinuum multispectral imaging in the long-wavelength region beyond the capabilities of ZBLAN fibers, enabled by a chalcogenide (ChG) fiber-based SC source in combination with a point scanning approach. We demonstrate tissue imaging in the diagnostically important fingerprint region from 5.7 µm (1754 $cm^{-1}$) to 7.3 µm (1370 $cm^{-1}$), and compare the results to those obtained using a commercial FTIR system.

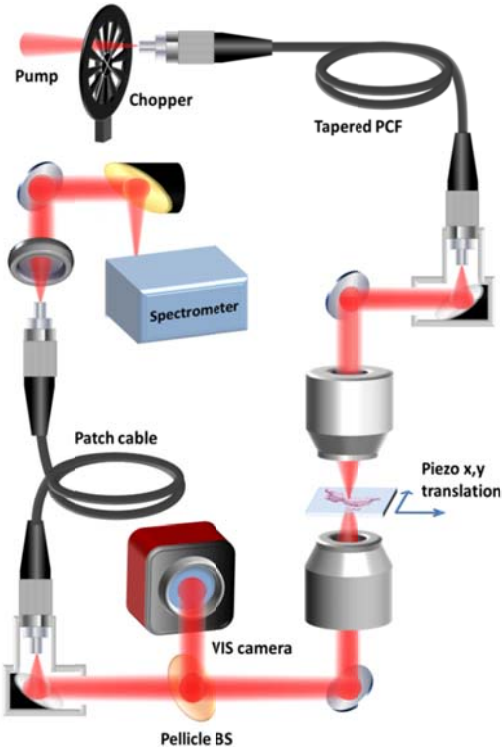


Fig. 1. Multispectral supercontinuum imaging system. Broadband SC light was generated in a tapered ChG PCF, and coupled via a fiber-optic connector (FC) interface to the scanning system. The sample was aligned to a 15x Cassegrain microscope using a CMOS camera, and imaging was realized by point-scanning using a piezoelectric translation stage. The signal was relayed via a ChG patch cable to a grating spectrometer for wavelength selection, and measured using an lock-in amplified MCT detector locked to the frequency of the chopper.

The experimental setup used for mid-IR multispectral imaging is detailed in Fig. 1. The SC was generated by pumping a tapered large mode area ChG photonic crystal fiber (PCF) with 250 fs pulses at 4.3 μm from a single-pass MHz optical parametric amplifier in order to obtain broad bandwidth, high average power, and single-mode output for the best possible imaging properties [11]. The fiber was end-capped and fitted with FC connectors for better environmental stability, robustness, and ease of coupling to the scanning system (see Fig. 2(a)). The tapered fiber was designed to have a short down-taper transition beginning after only a few cm of fiber, and a short waist section to reduce the effect of normal dispersion and confinement loss, respectively [11]. The taper profile and generated SC spectrum is shown in Fig. 2(b,c). The spectrum of the source was limited to spanning 2-7.5 μm with 25 mW output power due to a combination of design compromises. First of all, the need for end-capping and connectorization meant that a fiber with a smaller core diameter of 11.5 μm and pitch-to-hole-ratio of 0.45 was used, and secondly a long length of ~90 cm of uniform fiber was kept after the taper to allow for added flexibility, resulting in increased coupling-, confinement-, and propagation losses, respectively [11]. For tissue imaging the beam was long-pass filtered at 4.5 μm, allowing around 9-10 mW of power to be focused onto the sample.

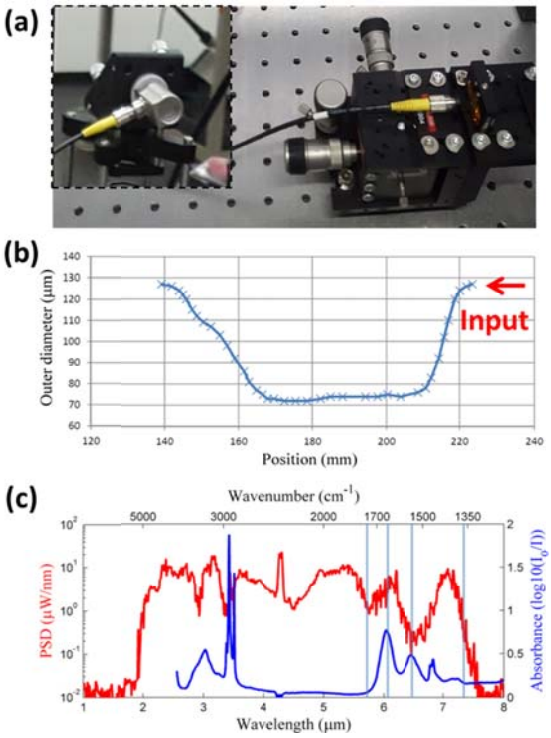


Fig. 2. (a) Picture of the free-space pump coupling to the tapered ChG PCF. The insert shows the fiber-coupling to the scanning system. (b) The taper profile having ~15 mm down-taper, ~40 mm waist, and ~30 mm up-taper. (c) The SC power spectral density (red) and typical colon sample FTIR absorbance (blue) spectra with light-blue horizontal bars to indicate the measured wavelengths.

The output end of the fiber was directly connected to the scanning system through an FC parabolic mirror collimator (see insert of Fig. 2(a)) and directed to a 15x Cassegrain transmission microscope with numerical aperture (NA) of 0.3, resulting in a diffraction-limited resolution of around 0.61λ/NA=12.4 μm at a wavelength of 6 μm. Imaging was realized by raster-scanning the sample at the beam focus in 5 μm steps over a 600 x 600 μm region using a piezoelectric translation stage. A broadband pellicle 50/50 beam splitter was placed in the beam path to allow for visual alignment of the sample with respect to the microscope using both a white LED and a fiber-coupled red laser. The remaining signal was subsequently focused into a 150 μm core diameter ChG patch cable, which relayed the signal to a grating spectrometer equipped with a mercury-cadmium-telluride (MCT) detector. The signal was chopped at 4 kHz in order to use lock-in detection with 50 ms time constant for maximum dynamic range. This limited the acquisition rate to 100 ms in order to avoid motion artifacts, which resulted in a 24 minute acquisition time for a single-wavelength point-scan image. During the scan the laser exposure remained around 15 times below than the maximum permissible exposure (MPE) level recommended for skin in the IEC 60825-1:2014 international standard and no effects due to heating of the tissue were observed.

The sample was a non-tumoral colon tissue section obtained from the Gloucestershire Royal Hospital with the approval of the local research ethics committee for collection of additional biopsies during routine clinical investigation by colonoscopy. After formalin

fixation and paraffin embedding, two sections were cut from this block. The 7 μm thick section was used for mid-IR imaging and the adjacent 3 μm section was used for gold-standard haematoxylin and eosin (H&E) staining on a glass slide and examined by an expert pathologist. The 7 μm thick section was mounted on a calcium fluoride ($CaF_2$) substrate, and measured directly without any chemical de-paraffinization. The H&E image seen in Fig. 3(a) displayed a typical normal tissue structure consisting of the epithelial glands (colonic crypts) with darkly stained outer nuclear regions, lightly stained inner cytoplasmic regions, connective tissue, thin muscle layer and mucin secretions. To be useful in pathology, a mid-IR imaging system must be able to identify these histological regions of the tissue based on the molecular features, most importantly the epithelial regions that are directly associated with cancer development, and the connective tissue. For this reason imaging was performed at 5.70 μm, 6.03 μm, 6.45 μm, and 7.30 μm, equivalent to 1754 $cm^{-1}$, 1658 $cm^{-1}$, 1550 $cm^{-1}$, and 1370 $cm^{-1}$, respectively. The choice of wavelengths was linked to some of the key molecular absorption features of the sample tissue whose shape and intensity can be related to cancer. These include the two major Amide I and II protein bands at ~6.03 μm and 6.45 μm, respectively, the lipid ester bonds around 5.7 μm, and the C-H bending vibration near 7.3 μm, which is also close to the detection limit of the setup. These are shown as horizontal bars in Fig. 2(c)).

Fig. 3(b) shows a visible light transmission mosaic image of the sample obtained through the scanning system, and Fig. 3(c-e) shows the corresponding mid-IR SC point-scan images at 6.03 μm, 6.45 μm, and 7.30 μm, respectively. The spectral-spatial mapping of these discrete frequency images are visualized in a composite image in Fig. 3(f), which distinguish the amide rich nuclear regions of the colonic crypts (c,d) from the surrounding connective tissue. The SC images were then compared with those obtained from a bench-top FTIR imaging system (Agilent 620 FTIR microscope coupled with an Agilent 670 FTIR spectrometer) consisting of a Globar light source, and a 128 x 128 MCT focal-plane array (FPA) detector. The FTIR spectral images were obtained using a 15x IR objective of NA 0.62 (a 7x final magnification is obtained at the sample plane due to ~2x de-magnification after the 15x objective) resulting in a pixel size of 5.5 x 5.5 $\mu m^2$ on the FPA detector. Images with a spectral resolution of 4 $cm^{-1}$ were obtained by averaging over 64 scans, and the full hyperspectral cube took 5 minutes to acquire plus an additional 15 minutes to complete 256 background scans.

The image contrast and intensity fluctuations were analyzed from line traces using a roughness calculation tool from the open source data visualization and analysis tool Gwyddion, and the results are presented in Fig. 4. The comparison reveals reduced contrast in the SC images compared to the FTIR images, which is to be expected from the larger spot size and oversampling. Since the imaging system is diffraction limited, the contrast and resolution could be improved by employing a 0.65 NA objective, resulting in an expected optical resolution of 5.6 μm. Other minor discrepancies in the apparent structure as imaged by the two systems could be due to the high spatial coherence of the SC beam.

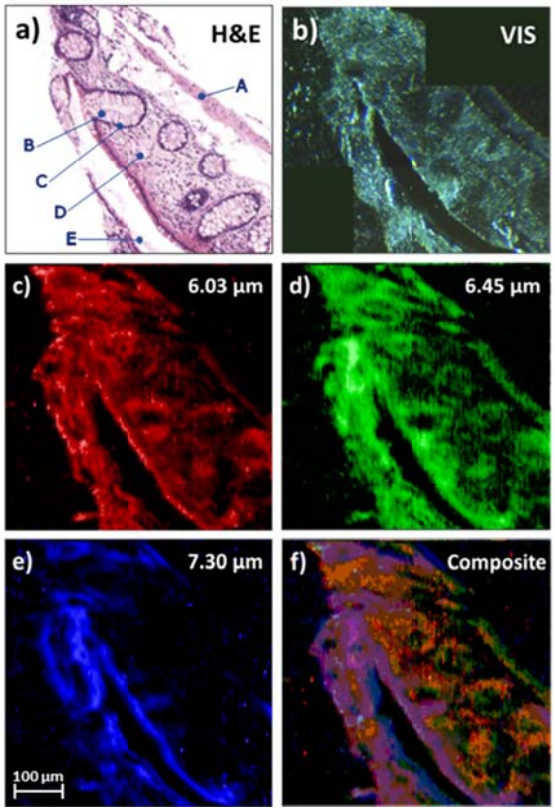


Fig. 3. Comparison between (a) the confocal image of the H&E stained tissue section with identification of the various histological regions. A: Muscle layer, B/C: cytoplasmic/nuclear regions of the colonic crypts, D: connective tissue, E: mucin secretions. (b) Visible light transmission image of the un-stained sample. (c,d) Mid-IR absorbance images of the protein rich amide regions highlighting the nuclear regions of the colonic crypts, and (e) the mucin secretions and surface epithelial walls. (f) Composite image showing the spectral-spatial mapping of c-e.

However, while the intensity fluctuations in the SC image was around 1.3 times higher than the corresponding FTIR image at 6.45 μm, they were more than 1.7 times lower in the SC image at 5.7 μm. This suggests that given sufficient power spectral density, relatively low-noise images can be produced using the SC scanning approach. Furthermore, the SC pump source was free-space coupled, which means that it was sensitive to drift over the 24 min acquisition time. Such coupling instability can be eliminated by switching to an all-fiber-based pump laser system [12]. The potential benefit of this method is that the entire broadband signal is passed through a small area of the sample, thus allowing for constant optical power on the sample with the highest possible SNR. Furthermore, the detection can be parallelized by switching from single-element to an array detector.

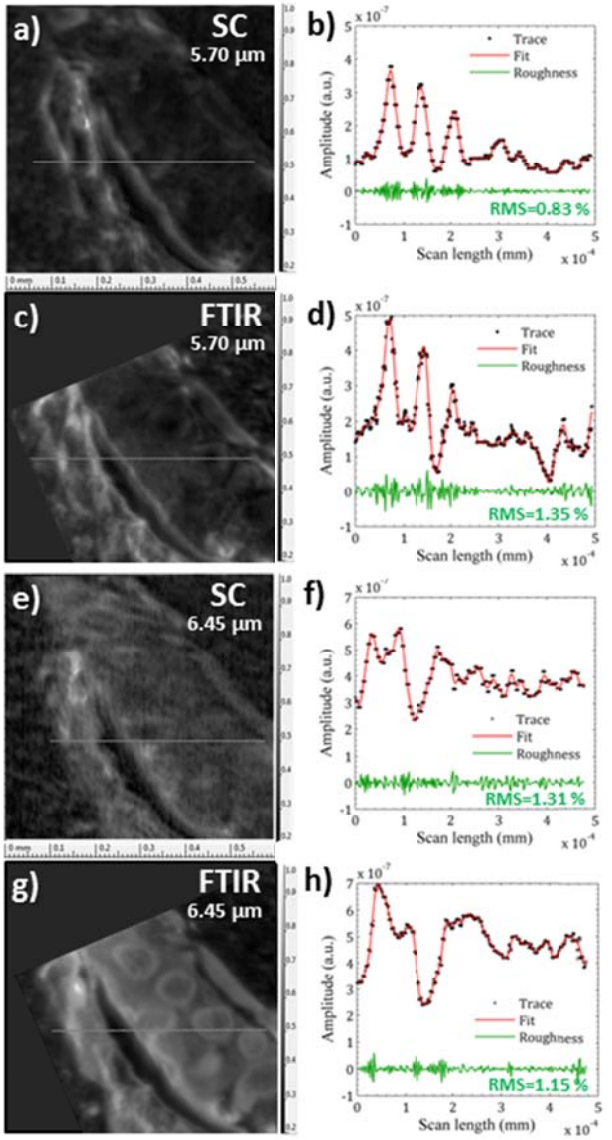


Fig. 4. (a,c,e,g) Mid-IR absorbance images measured at 5.7 µm and 6.45 µm using either SC or FTIR. (b,d,f,h) Contrast line traces corresponding to the lines in (a,c,e,g), and spatial noise analysis based on the roughness tool from the visualization and analysis software Gwyddion.

The bottle-neck of this method is the point scanning speed, which could be enhanced two orders of magnitude by operating the scanner in an open-loop configuration. This would allow the piezo to run constantly at full speed during acquisition, but requires a more elaborate hardware implementation and calibration. However, for imaging large sample areas or very small features the camera approach would be preferable. Such a system could be realized in a very small footprint by replacing the visible CMOS camera with an uncooled, broadband microbolometer camera, and exchanging the fiber-coupled spectrometer for an AOTF or broadband linear variable filter (LVF) for maximum throughput. With further development and availability of long-wavelength mid-IR components we expect the system to be able to match the acquisition rate of the 2.8-3.7 µm system reported in ref. [14], which was based on components that are now all commercially available.

In conclusion, we have demonstrated the feasibility of using a broadband fiber-coupled mid-IR SC source for multispectral tissue imaging in the spectral fingerprint region. This approach has shown that we can distinguish between epithelial and surrounding connective tissues within a paraffinized section of colon tissue by imaging at discrete wavelengths related to specific molecular absorption features.

**Acknowledgment**. The authors acknowledge Laurent Brilland of SelenOptics, and Johann Troles of Rennes University for fruitful discussions, and the fabrication and characterization of the tapered ChG PCF. The authors also acknowledge financial support from Taumoses legat.

**Funding.** Innovation Fund Denmark (4107-00011A); European Commission (FP7-ICT 317803).

## References

1. R. Baker, K. D. Rogers, N. Shepherd, and N. Stone, Br. J. Cancer **103**, 1034–1039 (2010).
2. J. T. Kwak, A. Kajdacsy-Balla, V. Macias, M. Walsh, S. Sinha, and R. Bhargava, Sci. Rep. **5**, 8758 (2015).
3. D. C. Fernandez, R. Bhargava, S. M. Hewitt, and I. W. Levin, Nat. Biotechnol. **23**, 469–474 (2005).
4. J. Nallala, M.-D. Diebold, C. Gobinet, O. Bouché, G. D. Sockalingum, O. Piot, and M. Manfait, The Analyst **139**, 4005–4015 (2014).
5. B. Guo, Y. Wang, C. Peng, H. L. Zhang, G. P. Luo, H. Q. Le, C. Gmachl, D. L. Sivco, M. L. Peabody, and A. Y. Cho, Opt. Express **12**, 208–219 (2004).
6. K. Yeh, S. Kenkel, J.-N. Liu, and R. Bhargava, Anal. Chem. **87**, 485–493 (2015).
7. N. Kröger, A. Egl, M. Engel, N. Gretz, K. Haase, I. Herpich, B. Kränzlin, S. Neudecker, A. Pucci, A. Schönhals, and others, J. Biomed. Opt. **19**, 111607–111607 (2014).
8. M. J. Pilling, A. Henderson, B. Bird, M. D. Brown, N. W. Clarke, and P. Gardner, Faraday Discuss **187**, 135–154 ( 2016).
9. P. Bassan, M. J. Weida, J. Rowlette, and P. Gardner, The Analyst **139**, 3856 (2014).
10. C. R. Petersen, U. Møller, I. Kubat, B. Zhou, S. Dupont, J. Ramsay, T. Benson, S. Sujecki, N. Abdel-Moneim, Z. Tang, D. Furniss, A. Seddon, and O. Bang, Nat. Photonics **8**, 830–834 (2014).
11. C. R. Petersen, R. D. Engelsholm, C. Markos, L. Brilland, C. Caillaud, J. Trolès, and O. Bang, Opt. Express **25**, 15336-15347 (2017).
12. D. D. Hudson, S. Antipov, L. Li, I. Alamgir, T. Hu, M. E. Amraoui, Y. Messaddeq, M. Rochette, S. D. Jackson, and A. Fuerbach, Optica **4**, 1163-1166 (2017).
13. T. Ringsted, H. W. Siesler, and S. B. Engelsen, Cereal Sci. **75**, 92–99 (2017).
14. M. Farries, J. Ward, I. Lindsay, J. Nallala, and P. Moselund, in Proc. of SPIE **10060**, 100600Y (2017).
15. S. Dupont, C. Petersen, J. Thøgersen, C. Agger, O. Bang, and S. R. Keiding, Opt. Express **20**, 4887–4892 (2012).
16. I. D. Lindsay, S. Valle, J. Ward, G. Stevens, M. Farries, L. Huot, C. Brooks, P. M. Moselund, R. M. Vinella, M. Abdalla, D. de Gaspari, R. M. von Wurtemberg, S. Smuk, H. Martijn, J. Nallala, N. Stone, C. Barta, R. Hasal, U. Møller, O. Bang, S. Sujecki, and A. Seddon, in Proc. of SPIE. **9703**, 970304 (2016).